CrossMark

RESEARCH ARTICLE

Portable tomographic PIV measurements of swimming shelled Antarctic pteropods

Deepak Adhikari[1] · Donald R. Webster[1] · Jeannette Yen[2]

Abstract A portable tomographic particle image velocimetry (tomographic PIV) system is described. The system was successfully deployed in Antarctica to study shelled Antarctic pteropods (*Limacina helicina antarctica*)—a delicate organism with an unusual propulsion mechanism. The experimental setup consists of a free-standing frame assembled with optical rails, thus avoiding the need for heavy and bulky equipment (e.g. an optical table). The cameras, lasers, optics, and tanks are all rigidly supported within the frame assembly. The results indicate that the pteropods flap their parapodia (or "wings") downward during both power and recovery strokes, which is facilitated by the pitching of their shell. Shell pitching significantly alters the flapping trajectory, allowing the pteropod to move vertically and/or horizontally. The pronation and supination of the parapodia, together with the figure-eight motion during flapping, suggest similarities with insect flight. The volumetric velocity field surrounding the freely swimming pteropod reveals the generation of an attached vortex ring connecting the leading-edge vortex to the trailing-edge vortex during power stroke and a presence of a leading-edge vortex during recovery stroke. These vortex structures play a major role in accelerating the organism vertically and indicate that forces generated on the parapodia during flapping constitute both lift and drag. After completing each stroke, two vortex rings are shed into the wake of the pteropod. The complex combination of body kinematics (parapodia flapping, shell pitch, sawtooth trajectory), flow structures, and resulting force balance may be significantly altered by thinning of the pteropod shell, thus making pteropods an indicator of the detrimental effects of ocean acidification.

1 Introduction

Aquatic locomotion methods range from the use of cilia or flagella for tiny microorganisms at very low Reynolds numbers ($Re = ul/\nu < 1$; Lauga and Powers 2009) to various types of undulating bodies and oscillating fins by larger fish at higher Reynolds numbers ($Re > 1000$; Lauder 2015), where u and l are the characteristic velocity and length scales, respectively, and ν is the fluid kinematic viscosity. Arguably, the most fascinating diversity in propulsion techniques is exhibited by zooplankton and larger invertebrates at intermediate Re. These techniques include jetting (e.g. jellyfishes, salps; Dabiri et al. 2006; Sutherland and Madin 2010), paddling (e.g. krill; Catton et al. 2011; Murphy et al. 2013), flapping (e.g. pteropods; Chang and Yen 2012), and clapping (e.g. scallops; Cheng and DeMont 1996).

In this work, the unique flapping mechanism of the shelled Antarctic pteropod (*Limacina helicina antarctica*; also known as the sea butterfly) is examined. The motivation for studying shelled Antarctic pteropod propulsion is twofold: (1) to provide a detailed understanding of their unique swimming characteristics for bio-inspired engineering and (2) to examine the possibility that their swimming modifications can serve as an indicator of ocean acidification (Bednaršek et al. 2012; Gattuso and Hansson 2011).

✉ Deepak Adhikari
deepak.adhikari@ce.gatech.edu

[1] School of Civil and Environmental Engineering, Georgia Institute of Technology, 790 Atlantic Drive, Atlanta, GA 30332, USA

[2] School of Biology, Georgia Institute of Technology, 950 Atlantic Drive, Atlanta, GA 30332, USA

1. *Unique swimming characteristics:* Fig. 1 shows an image of a shelled Antarctic pteropod (*L. helicina antarctica*), where its exterior consists of a dense aragonite ($CaCO_3$) shell and a pair of gelatinous parapodia (or "wings"). Pteropods swim upward in the water column by flapping their parapodia in a manner analogous to aerial flight. Due to the high density of the shell, the pteropod sinks if it does not flap continuously (Howes et al. 2014). Visual observations have shown that their swimming motion consists of power and recovery strokes of the parapodia, oscillatory pitching of the shell, and a sawtooth-like body trajectory (Chang and Yen 2012; Murphy et al. 2016). Furthermore, the flapping motion of the parapodia has also been argued to consist of attributes that may be similar to insect flight at intermediate *Re* (Murphy et al. 2016). These characteristics make the propulsion mechanism of pteropods unique compared to other aquatic organisms swimming in the intermediate *Re* range.

2. *Pteropod as indicator of ocean acidification:* Shelled pteropods, *L. helicina antarctica* (Fig. 1), are reported to be indicators of ocean acidification, OA (Orr et al. 2005). Pteropods precipitate calcium carbonate from seawater to create their aragonite shell. However, with OA, the ocean becomes undersaturated with calcium carbonate minerals preventing pteropods from producing and maintaining their aragonite shell (Gattuso and Hansson 2011). The result is shell thinning that alters the weight distribution and buoyancy of the organism. Pteropods that dwell in the Polar Regions are especially vulnerable to OA, since ocean water in these regions dissolves more carbon dioxide, and thus, the Polar Regions are more undersaturated with calcium carbonate than other areas (Gattuso and Hansson 2011). Previous work has demonstrated that pteropod shells in the Antarctic or Arctic regions have already been affected by increasing OA (Bednaršek et al. 2012; Comeau et al. 2012). A recent study has demonstrated that high concentration of carbon dioxide and decreased salinity affects the ability of pteropod to swim upwards (Manno et al. 2012). However, the detailed swimming mechanism of pteropods was not discussed. Therefore, quantifying the current state of pteropod swimming behavior is important, and com-

Fig. 1 a Image of a swimming shelled pteropod (*L. helicina antarctica*). The body exterior mainly consists of the parapodia ("wings") and the aragonite ($CaCO_3$) shell. **b** Schematic diagram of the pteropod with the defined chord, wing span, shell diameter, and leading and trailing edges of the parapodia
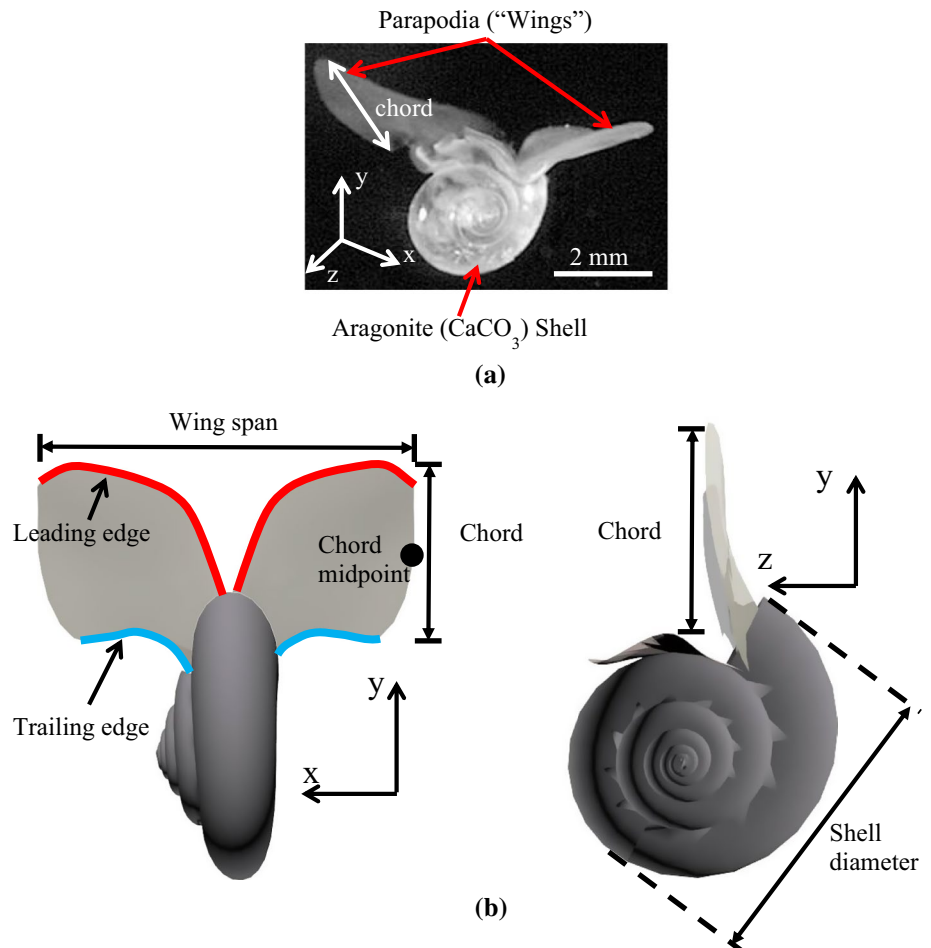
paring future swimming behaviors can potentially indicate the detrimental effects of OA.

Conducting an experiment on healthy pteropods is challenging, since they are unable to survive in a laboratory for a long period of time (Howes et al. 2014). Furthermore, for Antarctic pteropods, the seawater has to be consistently kept at low temperatures close to 0 °C to match habitat conditions. Thus, it is not surprising that there are limited previous studies dedicated to the swimming behavior of Antarctic pteropods, despite being in abundance in the Southern Ocean. One of the earlier works on swimming pteropods examined the characteristics of an Antarctic shell-less pteropod (*Clione antarctica*; Childress and Dudley 2004). Unlike shelled pteropods, the shell-less species do not sink and are almost neutrally buoyant. Childress and Dudley (2004) found two methods of locomotion in this shell-less species: (1) use of cilia bands around their body and (2) reciprocal flapping parapodia. They hypothesized that there is a *Re* range from 5 to 20 (based on body length and swim speed) in which the shell-less pteropods switch from cilia propulsion mode (*Re* < 5) to flapping mode (*Re* > 20). Shelled pteropods (*L. helicina antarctica*), however, do not have cilia bands, are negatively buoyant, and propel only with their flapping parapodia. Chang and Yen (2012) studied free-swimming and tethered shelled Pacific pteropods (*L. helicina*) and noted that the flapping parapodia and their complex body motion may indicate a unique propulsion mechanism. Although the kinematics of the tethered pteropod was described, Chang and Yen (2012) did not provide details of the propulsion mechanism. Furthermore, tethered specimens substantially modify their true kinematics due to constraints on their body movement (e.g. lack of shell pitching, and changes in flapping frequency). More recently, Murphy et al. (2016) explained that the shelled Pacific pteropod (*L. helicina*) exhibits propulsion characteristics that are similar to insect flight. These include a near Weis-Fogh "clap-and-fling" mechanism to augment lift (Lighthill 1973; Weis-Fogh 1973) and a figure-eight parapodia trajectory that is facilitated by "hyper-pitching" of the shell (Murphy et al. 2016). Among all aforementioned studies, only Murphy et al. (2016) conducted quantitative measurements of the flow field for a freely swimming pteropod. However, Murphy et al. (2016) did not elaborate the details on the relationship between shell pitching and parapodia flapping, and of the contributions of flow structures to the propulsion of the organism.

Particle image velocimetry (PIV) has been the major measurement tool to study propulsion and flow manipulation by aquatic organisms (e.g. Lauder 2015). With recent advances in volumetric velocimetry techniques, there have been significant efforts to develop techniques to quantify the inherently three-dimensional flow fields generated by aquatic organisms. These techniques include tomographic PIV (e.g. Adhikari and Longmire 2013; Murphy et al. 2012), volumetric three-component velocimetry (e.g. Flammang et al. 2011), synthetic aperture PIV (e.g. Mendelson and Techet 2015), and holography (e.g. Malkiel et al. 2003). Since aquatic organisms respond to light in the visible wavelength range, some of these works have incorporated infrared laser illumination to observe the natural behavior of organisms in the absence of photo-responses (e.g. Adhikari and Longmire 2013; Mendelson and Techet 2015; Murphy et al. 2012). Most multi-camera volumetric velocimetry techniques require an optical table, or a large and heavy bench, to ensure that components are sturdy and rigid to maintain a fixed alignment of all cameras during calibration and experiments. Obviously, transporting such platforms is often not practical for researchers seeking to perform measurements outside of the laboratory.

Since shelled Antarctic pteropods are extremely delicate to transport, it was important to develop a portable version of the measurement system that could be implemented in Antarctica to study the swimming behavior of these pteropods that dwell in the Southern Ocean. In this study, we describe a new portable infrared tomographic PIV system that was deployed at Palmer Station, Antarctica, to examine the shelled Antarctic pteropods (*L. helicina antarctica*). We investigate the kinematics and flow velocity field surrounding these pteropods and describe their swimming mechanisms and the surrounding flow structures.

2 Materials and methods

2.1 Species and environment

Shelled Antarctic pteropods (*L. helicina antarctica*; Fig. 1) were collected from Palmer Deep (64°57′S, 64°24′W) and Boyd Strait (62°50′S, 62°00′W) in the Southern Ocean using a plankton net with 2 m × 2 m rim size and 500 µm mesh size. Specimens were collected on board a research vessel, *RV* Laurence M. Gould, en route to Palmer Station (Anvers Island, Antarctica; 64°46′S, 64°03′W) in November 2014. Once collected, organisms were housed in large buckets of seawater with salinity of 34.6 parts per thousand (ppt), stored at 0 °C, and transported to the station where experiments were conducted. A 2-week limit for experiments was imposed to ensure healthy specimens were studied since pteropods do not feed well in a confined environment. New batches of pteropods were collected every 2 weeks following the initial collection. Among those collected, adults in the size ranging from 1.5 to 5 mm were used for the experiments.

Fig. 2 **a**, **c**, **d** Solidworks® CAD images, and **b** an image of the experimental setup at Palmer Station, Antarctica. The frame components highlighted in *red* position the cameras along the *z*-axis. The frame components highlighted in *blue* and *green* position are the tank and laser along the *y*-axis, respectively. The *double arrows* in **d** indicate the direction that the frame components can slide. The flat rails facilitate sliding the laser and cameras for additional alignment
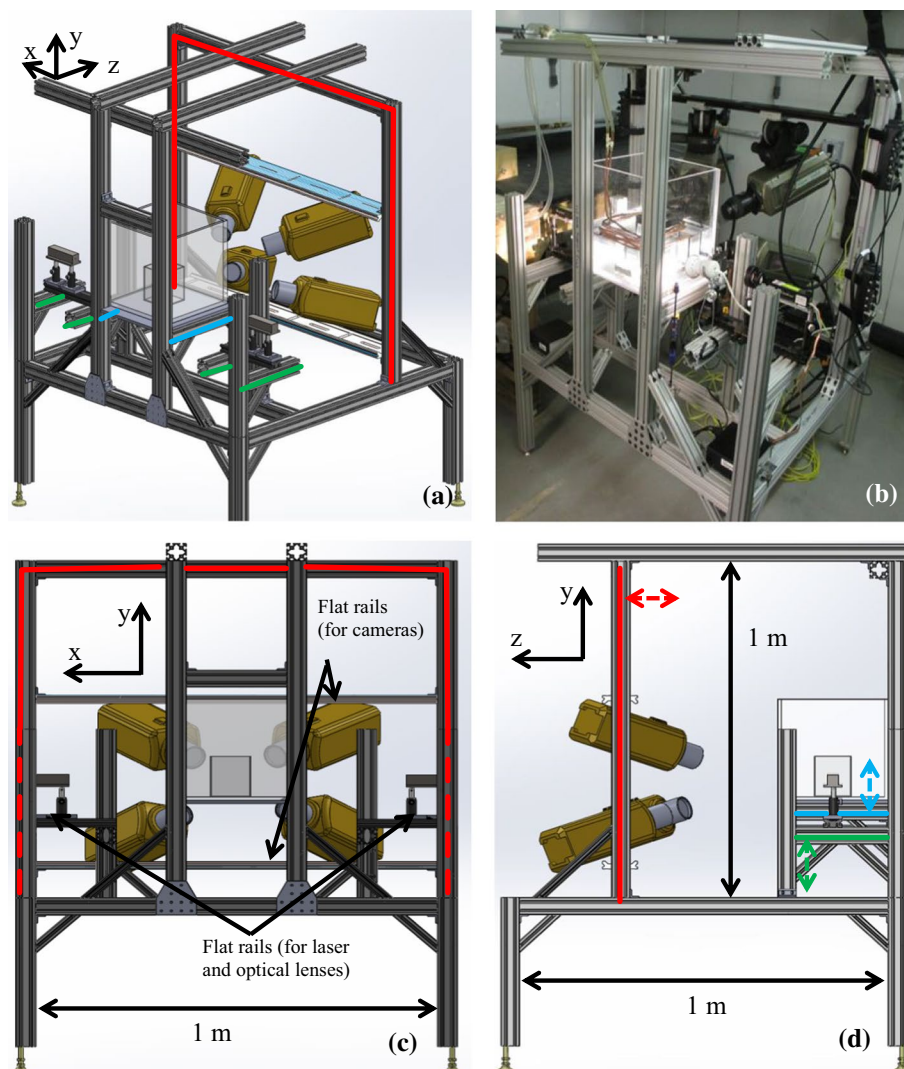
2.2 Experimental setup

2.2.1 Portable frame

A single portable frame was designed to rigidly support the cameras, lasers, and tanks (see Fig. 2). Figure 2a shows the computer-aided design (CAD) image of four cameras, two lasers, and the tank assembly mounted within the frame. The frame is self-contained with all components of the tomographic PIV system without the need for heavy and bulky equipment (e.g. optical table, work bench). Figure 2b shows a picture of the experimental setup in a temperature-controlled room at Palmer Station. The frame components highlighted in red, blue, and green are adjustable to allow alignment of the lasers, cameras, and tanks (see Fig. 2a, c, d). The axes are defined as shown in Fig. 2.

The cameras' position can be adjusted in all axis directions. The frame components highlighted in red slide in the *z*-axis. This allows adjustment of the distance from the cameras to the tanks. The flat rails supporting the cameras can slide in the *y*-axis, and the camera mounts attached to the flat rails allow the cameras to slide in the *x*-axis. The tank assembly can traverse in the *y*-axis by moving the frame components that support the tank (frame components highlighted in blue). This allows the tank to be placed at an appropriate height relative to the cameras. The frame components highlighted in green (adjustable in the *y*-axis), together with the optical rails (adjustable in *x* and *z* axes), allow the laser and the optical lenses to be positioned in all axis directions. This enables proper alignment of the laser with the test section within the tank assembly.

The portable frame was assembled with *T*-slot profile optical rails (80/20 Inc.; cross section: 50.8 × 50.8 mm), and the cameras and lasers were mounted on flat rails (Qioptiq Photonics GmbH; Melles Griot). The length of each rail was not longer than 1 m to facilitate easy packing and transport (see Fig. 2c, d). When disassembled, all the rails fit into two golf club cases (130 × 40 × 40 cm) that

can be transported as check-in baggage onboard any commercial passenger aircraft.

2.2.2 Tank assembly

A glass test tank measuring $10 \times 10 \times 12$ cm (W × D × H) was filled with seawater to a height of 10 cm. Filtered seawater was obtained directly from the coastal ocean waters near Palmer Station. The tank was placed in a transparent acrylic glycol–water bath tank ($30 \times 30 \times 30$ cm) with a closed-loop heat exchanger coil to maintain the temperature of the seawater at 0 °C throughout the experiment (Fig. 3). The ambient temperature of the room was 10 °C, which was reasonably comfortable for the researcher to conduct experiments for extended periods of time. The pteropods generally sink to the bottom of the tank due to their dense shell and swim up by flapping their parapodia. The field of view was at least 30 mm above the bottom of the tank such that only actively swimming pteropods appear in the recordings.

2.2.3 Procedure

Prior to the experiment, pteropods that were swimming actively in the large buckets were separated from the weakly swimming ones. A small cup was then submerged into the bucket, and the actively swimming pteropod was allowed to move freely into the cup. The cup was lifted from the bucket and carefully submerged into the test tank where the pteropod was again allowed to swim freely out of the cup. Care was taken to avoid any splashing while transferring these delicate specimens from the bucket to test tank. Approximately 5–8 pteropods of various sizes were placed concurrently within the test tank before data acquisition commenced.

2.3 Infrared tomographic PIV and kinematics methodology

Infrared high-speed tomographic PIV (Adhikari and Longmire 2013; Murphy et al. 2012) was applied to quantify the volumetric velocity field surrounding the swimming pteropod. This multi-camera system also enables kinematics measurements of the parapodia and shell motion of the pteropod. The measurement volume was illuminated with two 7 W continuous-wave infrared lasers (CrystaLaser, Inc.) with wavelength of 808 nm (see Fig. 3). Infrared illumination was selected since zooplankton typically cannot sense light at this wavelength and therefore do not modify their swimming behavior during observation (Adhikari et al. 2015; Catton et al. 2007; Murphy et al. 2012). The lasers were placed on either side of the tank with overlapping illumination volumes to prevent "shadowing" by the
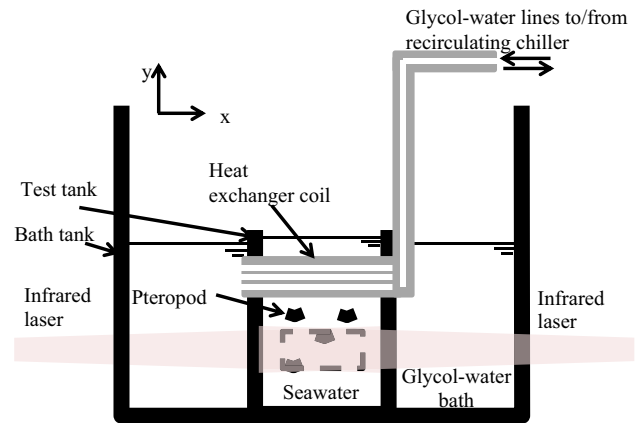

Fig. 3 Schematic design of the tank assembly. The test tank filled with seawater is located inside the bath tank filled with 50% glycol and 50% water. A recirculating heat exchanger coil is wrapped around the test tank to maintain the temperature of seawater inside the test tank at 0 °C

pteropod (Fig. 3). The beams were expanded into a volume with height (y-axis) and thickness (z-axis) of 19 and 13 mm, respectively, at the measurement region. Four high-speed cameras (Vision Research Inc. Phantom v210; 1280×800 pixels), fitted with Scheimpflug mounts (LaVision GmbH Model #1108196) and 105 mm lens (Nikon Micro-NIKKOR), were mounted on three-axis geared heads (Manfrotto 400) and secured on the flat optical rail. The cameras were angled at approximately 30° to the z-axis and aimed at the measurement volume (Fig. 2). The recordings in all cameras were synchronized at 500 fps, and the camera lens aperture was set to f/11. The test tank was seeded with 20 µm polyamide (1.03 g/cm³) tracer particles (Orgasol 2002 D NAT 1; Arkema Group). These particles scatter the infrared illumination and are inert to pteropods. Experiments were conducted with new sets of organisms and particles daily to ensure recordings of healthy swimming behavior and to prevent particles from agglomerating.

A calibration plate was traversed to six positions spanning the z-axis of the measurement volume, and a preliminary mapping function was determined from the resulting calibration images. A self-calibration procedure reduced disparity errors and hence corrected the calibration mapping function for all cameras leading to a reduced calibration error (Wieneke 2008). For tomographic PIV, particle intensity volumes were reconstructed using the MLOS-CSMART algorithm implemented in DaVis 8.2 (LaVision GmbH). This resulted in a measurement volume of -16 mm $< x < 16$ mm, -7 mm $< y < 12$ mm and 0.5 mm $< z < 13.5$ mm. A visual hull technique was applied to prevent vector contamination near the organism (Adhikari and Longmire 2012). The volume of velocity vectors was calculated by cross-correlating reconstructed volume
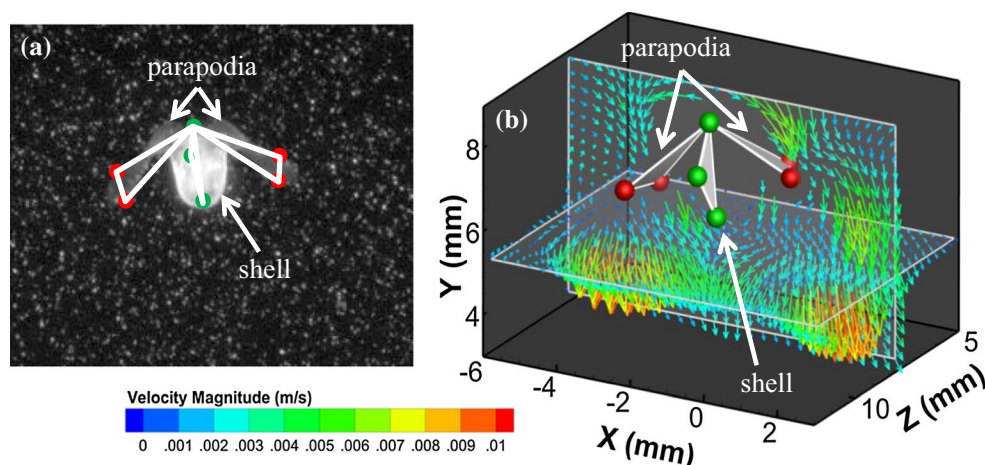
Fig. 4 a Image from one of the cameras where the *circles* indicate the marker points for 3D kinematics and **b** corresponding volumetric fluid velocity field from infrared tomographic PIV where the spheres represent the volumetric locations of the *circles* in **a**. *Note:* that the dimensions of the volumetric vector field were reduced to highlight the flow around the pteropod

pairs separated by $\Delta t = 10$ ms (i.e. every five volumes). The smallest interrogation volume yielding high-quality results was $32 \times 32 \times 32$ voxels. Using a 75% overlap, the correlated vectors resulted in volumetric fields of $97 \times 58 \times 39$ vectors and a vector grid spacing of 0.33 mm. The uncertainty in the velocity measurements was estimated to be 0.8 mm/s.

To quantify the organism kinematics, the location of seven (7) marker points on the body of the pteropod were manually estimated in each of the four simultaneous images (see Fig. 4a). Similar approaches of employing marker points for kinematics analysis have been used previously for copepods (Murphy et al. 2012) and fish (Mendelson and Techet 2015). In the current work, the markers include three (3) points (green) on the circumference of the shell and four (4) points (red) on the distal ends of the parapodia (two on each parapodium). Using the same calibration plate images as the tomographic PIV, a direct linear transformation operation (Hedrick 2008) was applied to triangulate the three-dimensional location of each point. The error of identifying marker location in the x- and y-axes was estimated to be 0.1 mm and in the z-axis was estimated to be 0.2 mm. The resulting vector field from the tomographic PIV operation and the organism position from the 3D kinematics were combined in Tecplot (TecPlot Inc.) for visualization and analysis (e.g. Fig. 4b).

3 Results and discussion

3.1 Implementation of the measurement system

In this experiment, the infrared laser light traveled through a bath tank before illuminating the particles in the test tank
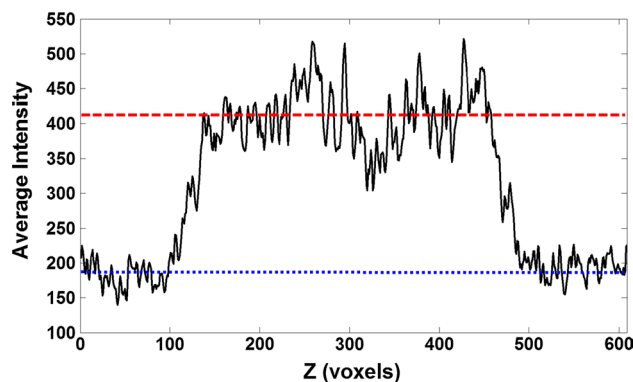

Fig. 5 Average intensity profile across the *z*-axis to indicate the SNR (signal: *dashed line*, noise: *dotted line*). The SNR is > 2 on average, which is sufficient for tomographic PIV reconstruction

(see Fig. 3). Since infrared light attenuates in water, the use of the infrared laser and the additional distance required for the illumination to travel through the bath tank can contribute to a low-quality image (i.e. reduced signal). Therefore, the signal-to-noise ratio (SNR) of the reconstructed volume was evaluated a posteriori. The SNR is assessed as the ratio between the average intensity levels measured within the volume illuminated by the laser and the levels measured outside of it (Elsinga et al. 2006; Scarano and Poelma 2009). This gives the ratio between actual particle and ghost particle intensities. For the current experiment, the reconstructed intensity averaged over the *z*-direction is 410 within the illuminated volume (Fig. 5; dashed line), whereas the reconstructed intensity outside of the illuminated volume due to ghost particles (noise) is 180 (dotted line). This yields a reconstruction SNR of 2.3. A ratio of 2 has been reported to be sufficient for tomographic PIV
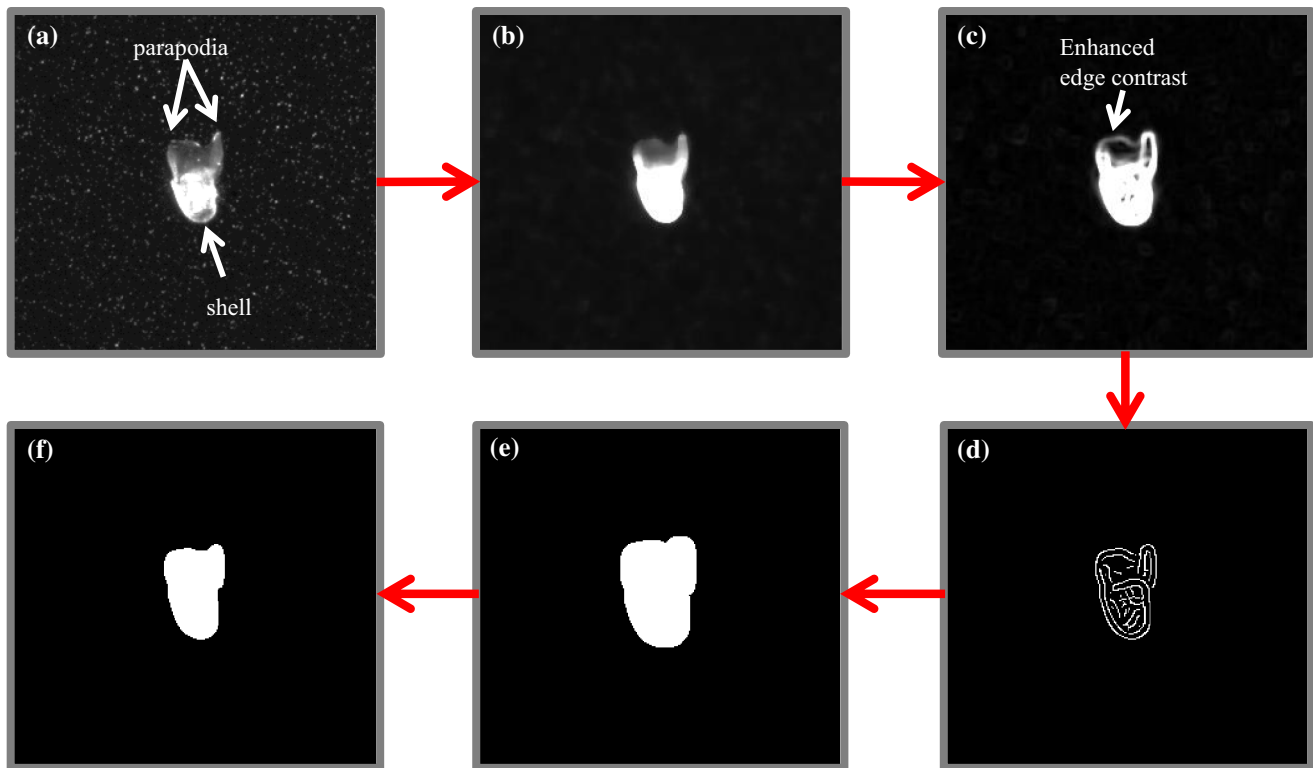
Fig. 6 Automated image processing sequence to obtain the silhouette of the pteropod required for constructing the visual hull. **a** Original image, **b** image after applying median filter to neighboring 7 × 7 pixels, **c** image after applying standard deviation filter to neighboring 5 × 5 pixels, **d** image after applying Canny edge detection with two gradient thresholds for locating and tracing the edges, **e** image after applying morphological dilation and filling to neighboring pixels, and **f** image after applying morphological erosion

reconstruction (Elsinga et al. 2006; Scarano and Poelma 2009; Casey et al. 2013). Based on this assessment, we find that the combination of the current infrared illumination, seeding particles, and tank assembly is sufficient for accurate reconstruction of particle volumes from a set of four projected images.

Another concern using the current system is that the appearance of the pteropod in the camera images can create artifacts when the images are reconstructed into volumes. These artifacts contaminate the velocity vector field surrounding the organism. The visual hull method was used as a mask to remove the organism artifact that appears within the reconstructed volume (e.g. Adhikari and Longmire 2012; Langley et al. 2014; Mendelson and Techet 2015; Murphy et al. 2016). Adhikari and Longmire (2012, 2013) recommended an image processing sequence that was used to obtain the silhouette of dark objects and fish, respectively, before back-projecting the silhouettes to construct the visual hull. In this case, modification to the image processing sequence was necessary, since the recommended sequence could not be used to detect the translucent parapodia of the pteropods. It is also desirable to avoid the time-intensive manual tracing of the translucent parapodia employed in the study of Pacific pteropods (Murphy et al.

2016). Furthermore, illumination reflected off the pteropod shell also contributed to image noise by diminishing the contrast of nearby illuminated particles. Thus, for this study, a different image processing sequence was used to detect the silhouette of the pteropod.

Figure 6a shows a raw image that was obtained directly from one of the cameras, where the translucent parapodia, bright shell, and surrounding particles can be observed. A median filter with a 7 × 7 pixel window was applied to filter away the tracer particles (Fig. 6b). A standard deviation filter with 5 × 5 pixel window was then applied to enhance the boundaries of the parapodia for better edge contrast (Fig. 6c). Median and standard deviation filters replace each pixel with the median and standard deviation, respectively, of its neighborhood within the window. Canny edge detection was then applied to locate the edges of the object (Fig. 6d). Canny edge detection finds the spatial gradient in an image based on two user-defined gradient thresholds. Upon detecting an initial edge point based on the higher threshold, it tracks connected edge points using a lower threshold level, thus enabling it to detect weaker edges and minimizing the influence of noise or particles. In this case, the ratio between the upper and lower thresholds was sufficiently large at 25 (higher threshold: 0.01, lower threshold:
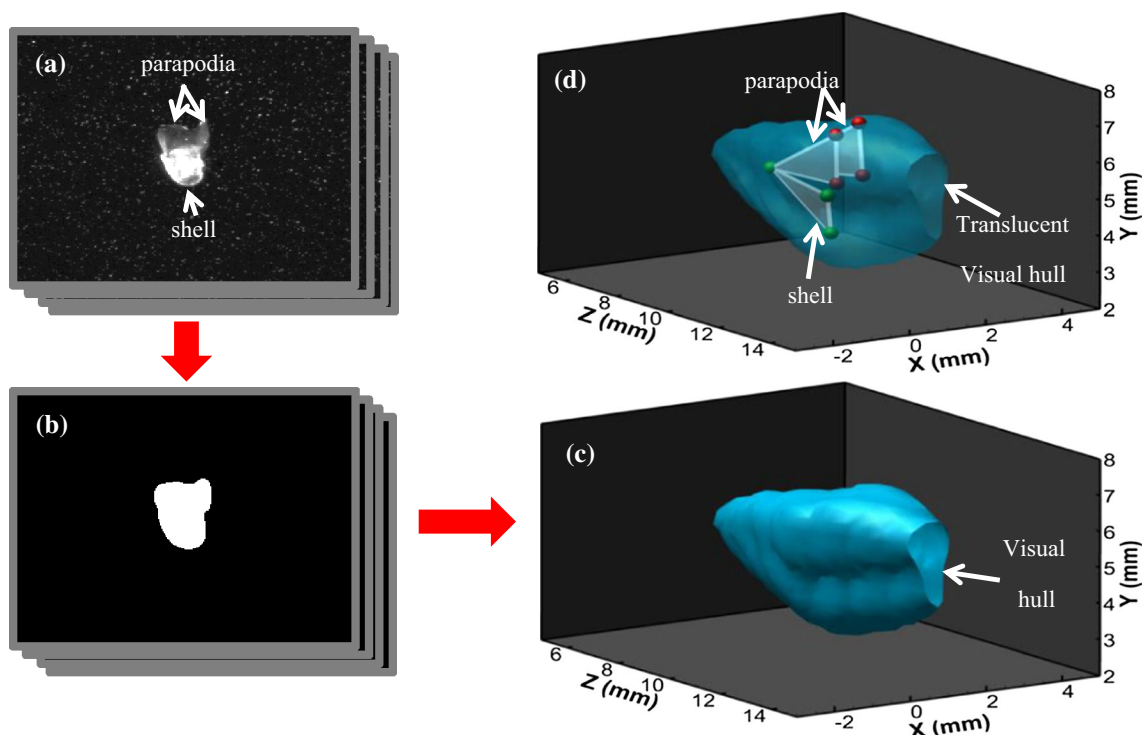
Fig. 7 Processing sequence from **a** images from 4 cameras, to **b** silhouettes, to **c** a visual hull of the pteropod. **d** Marker points of parapodia and shell shown within the translucent visual hull of the organism

0.0004) to enable detecting the edges of both the translucent parapodia and the brightly illuminated shell. Next, morphological dilation of 7 pixels was applied to increase the thickness of the detected edges, and filling was applied to add pixels to any background "holes" present within the object (see Gonzalez and Woods 2002; Fig. 6e). Finally, morphological erosion was applied to decrease the size of the dilated image by 5 pixels. The erosion was done with fewer pixels compared to dilation so that the final silhouette was slightly larger than the original organism. This was done to mask out noisy reconstruction near the pteropod shell caused by the illumination reflecting off the shell (Fig. 6f).

The processing sequence described above was applied to the four simultaneous images, and the corresponding silhouette was obtained for each of them (see Fig. 7a, b). A MLOS algorithm within DaVis 8.2 was used to obtain a visual hull of the silhouettes (Fig. 7c). The use of visual hull masking on the reconstructed particle volume avoids contaminated vectors during cross-correlations. However, due to the complex geometry and swimming pattern of the pteropod, the visual hull does not provide a reasonable indication of the pteropod shell and parapodia orientation. Thus, kinematics tracking of the parapodia and shell were superposed to provide better visualization of the pteropod

kinematics compared to the visual hull during analysis (Fig. 7d).

3.2 Swimming kinematics

3.2.1 Swimming sequence

Figure 8 shows the time sequence of a swimming pteropod flapping its parapodia during power (a–e) and recovery (f–j) strokes for Reynolds number, $Re_f = U_{tip}c/v = 80$, where U_{tip} is the parapodia (or "wing") tip velocity, c is the chord length of the parapodium, and v is the kinematic viscosity of seawater at 0 °C (see Movie_1.avi in supplementary material for the video of this time sequence). Typically, a power stroke is defined as the stroke that elicits propulsion, whereas the recovery stroke elicits little or no propulsion. However, in this case, thrust is produced during both strokes. Thus, we define the power stroke to be the stroke that begins with the parapodium touching each other (e.g. Fig. 8a). We find that the power stroke defined here consistently contributes more thrust than the recovery stroke. Figure 8a shows the start of the power stroke where the parapodia are almost "clapped" together, but a gap is observed between the parapodia. Typically, the distal ends of the parapodia either touch each other or overlap for
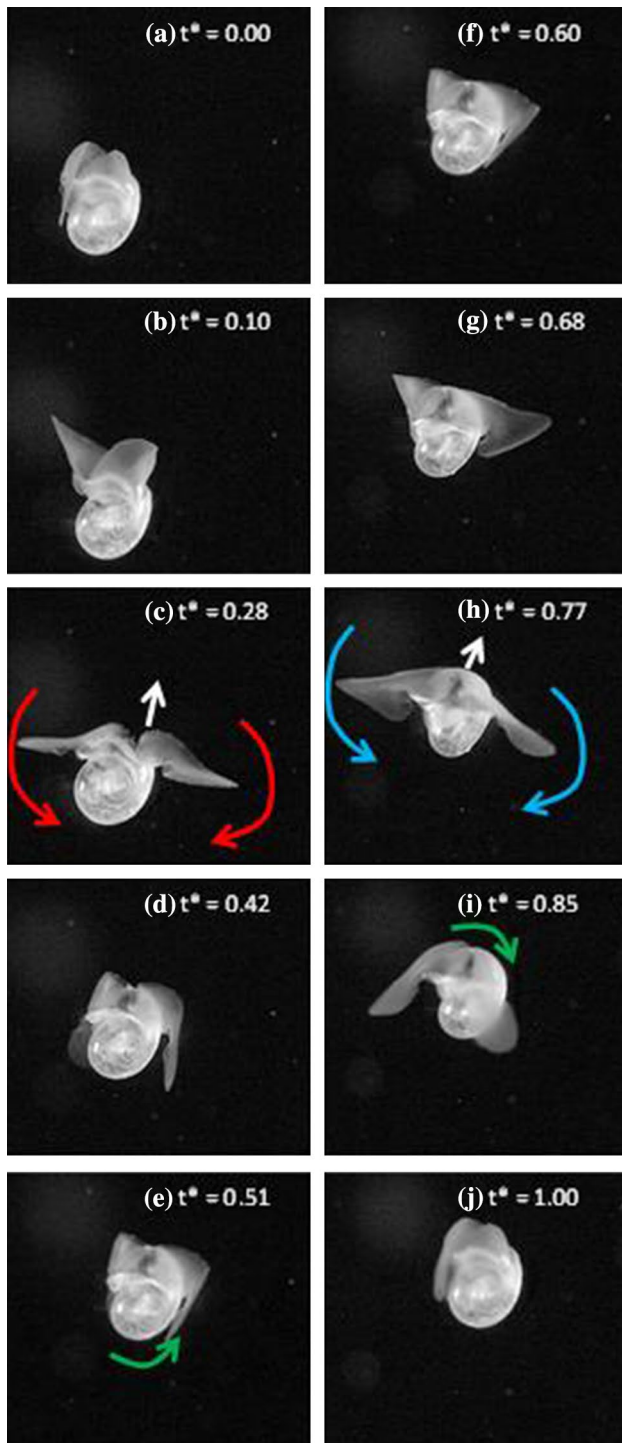
Fig. 8 Time sequence showing one complete cycle of power (**a–e**) and recovery (**f–j**) strokes of a pteropod during vertical swimming. The shell pitches during every stroke to reorient the parapodia position such that the next half-stroke is directed downwards. The *red arrows* highlight the downward flap during the power stroke, and the *blue arrows* highlight the downward flap during the recovery stroke. The *white arrows* indicate the translation motion, and *green arrows* highlight the shell pitching motion. Time, *t*, is normalized by the flapping cycle period, *T* (i.e. $t^* = t/T$)

shelled Antarctic pteropod. Overlapping parapodia was not observed for shelled Pacific pteropod (Murphy et al. 2016). In Fig. 8b, the parapodia are observed to initiate the power stroke. This downward power stroke (indicated by red arrow in Fig. 8c) results in an upward motion of the pteropod body (indicated by white arrow in Fig. 8c). In Fig. 8d, e, the parapodia are on the sides of the shell after the power stroke, and the shell has already started to pitch (green arrow). Figure 8f, g shows the parapodia starting their recovery stroke. The pitching of the shell in Fig. 8 causes the parapodia to reorient such that they flap downwards again during the recovery stroke (blue arrow in Fig. 8h). The recovery stroke causes the shell to move upwards again (white arrow in Fig. 8h) and pitch in the opposite direction (green arrow in Fig. 8i). Finally, the pteropod returns at the end of the recovery stroke (Fig. 8j) to a similar orientation as Fig. 8a, but is elevated due to the resultant upwards thrust. All observed cases of upward pteropod swimming are consistent with this sequence.

The described propulsion behavior is a case of flapping "wings" underwater, and a particularly unique characteristic of this swimming behavior is that both the power and recovery strokes flap downwards (e.g. Fig. 8c, h). This is in contrast to other organisms with reciprocal wing motion (e.g. shell-less pteropods, birds, and insects), in which their recovery stroke traverses in the opposite direction as that of the power stroke.

3.2.2 Shell trajectory and pitching

The mechanism of flapping downwards during both strokes can be attributed to the shell pitching. Figure 9ai shows an example of a shell trajectory during upward swimming of a pteropod. The shell centroid is observed to translate in a sawtooth-like trajectory. Power and recovery strokes are indicated by the colored arrows, respectively, in the zoomed-in view of Fig. 9ai. Both strokes contribute to the upward motion of the shell. Brief periods where the centroid appears to drop vertically correspond to the transition between the strokes (indicated by white arrows in the zoomed-in view of Fig. 9ai). This is a result of the shell sinking due to the weight, as there is no thrust acting during the transition between power and recovery strokes.

Figure 9a also shows the angular orientation (θ) of the pteropod shell during swimming, where θ is quantified as the angle between the y-axis and a line segment connecting the center of the shell to the proximal side of the parapodia. A time sequence of this angle quantifies the pitching extent of the shell during each stroke, which ranges from $-40°$ to $70°$ (Fig. 9ai). This range ($70° - [-40°] = 110°$) is large enough to cause reorientation of the parapodia such that both power and recovery strokes are directed downwards.
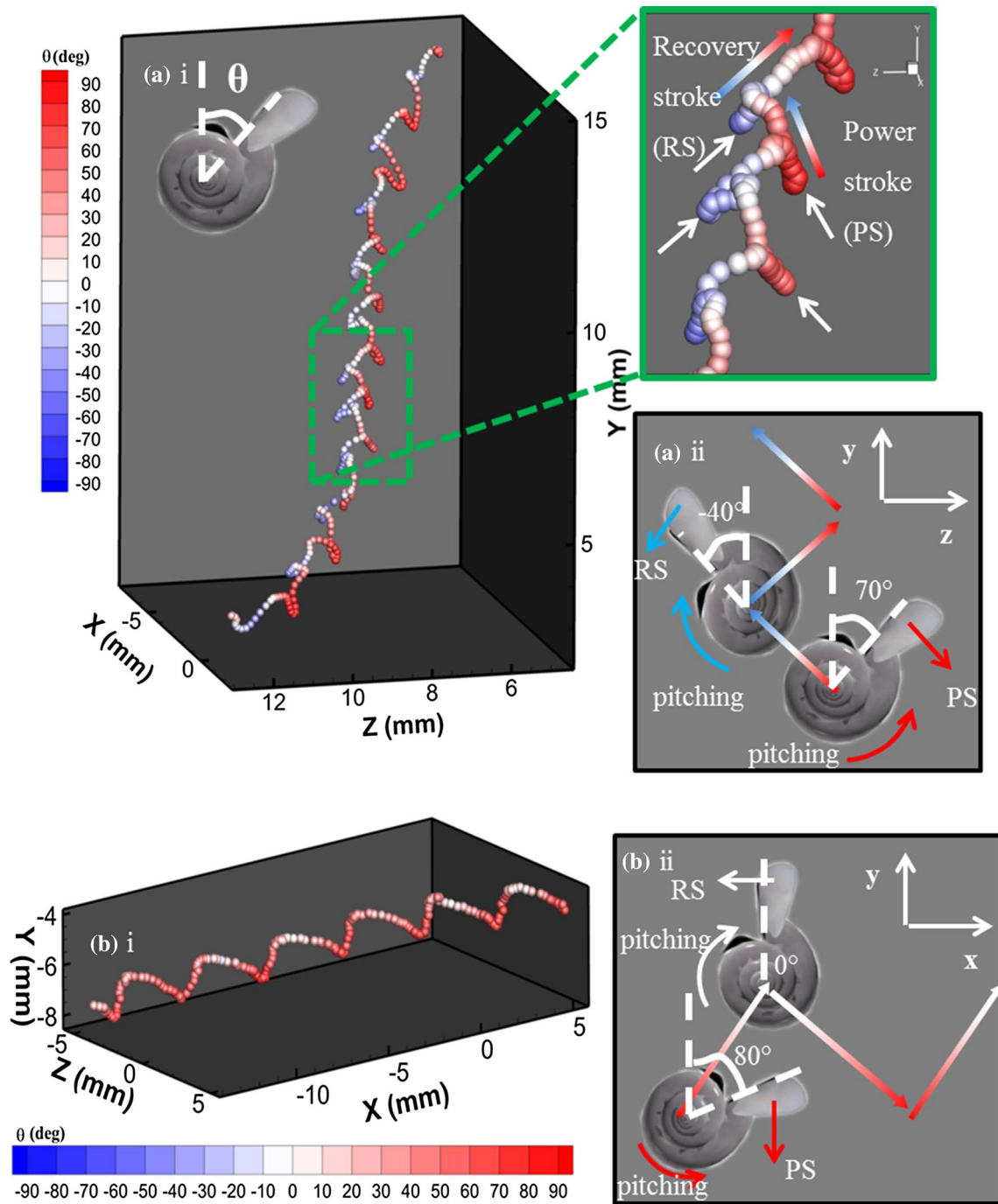
Fig. 9 a Vertical and **b** horizontal swimming. The angle, θ, is given by the angle between the *y*-axis and a line segment connecting the center of the shell to the proximal parapodia. **a** *i* Shell trajectory of a vertically swimming pteropod where the shell angular orientation ranges from 70° to −40° during power stroke and −40° to 70° during recovery stroke. **a** *ii* Schematic representation of a pteropod achieving upward swimming. **b** *i* Shell trajectory of a horizontally swimming pteropod, where the shell angular orientation ranges from 80° to 0° during power stroke, and 0° to 80° during recovery stroke. **b** *ii* Schematic representation of pteropod achieving horizontal swimming

It is worth noting that similar pitching is also observed in shelled Pacific pteropod where the angle range of up to 60° was documented by Murphy et al. (2016), but the mechanism of pitching was not described.

Figure 9aii provides a schematic illustration to describe how shell pitching enables the reorientation of the parapodia. The pteropod, initially at θ = 70°, initiates a power stroke (PS). During the power stroke, the pteropod

translates upwards and rotates (or pitches) because the force acting on the pteropod by the fluid is offset from the center of mass of the pteropod. The translation moves the pteropod upwards (and to the left), while pitching the shell to $\theta = -40°$. The pteropod initiates a recovery stroke (RS), which again translates the shell upwards (and to the right), and returns the shell back to angular orientation of $\theta = 70°$. From this analysis, we find that pteropods strategically use shell pitching to enable both power and recovery strokes to flap downwards such that the reaction force on the parapodia displaces the pteropods upward during both strokes.

Figure 9bi shows another trajectory of a swimming pteropod, where it is moving horizontally (in the x-direction) along a sawtooth-like trajectory. The angular orientation ranges from 0° to 80°. Figure 9bii shows a schematic representation of how the pteropod manages to move horizontally. The pteropod is initially oriented at $\theta = 80°$ at the beginning of the power stroke. During the power stroke, the pteropod translates upwards (and to the right) and pitches such that the shell orients to $\theta = 0°$. During the recovery stroke, however, the parapodia do not flap downwards since the stroke begins with $\theta = 0°$. Instead, the shell is positioned such that the parapodia flap to the left ($-x$-direction). Thus, the force acting on the pteropod during the recovery stroke is to the right ($+x$-direction). Since the shell is negatively buoyant, the resulting displacement of the pteropod during recovery stroke is to the right (and downwards). The recovery stroke pitches the shell back to $\theta = 80°$, and the pteropod returns to the beginning of the power stroke.

Figure 9a, b shows how a shelled Antarctic pteropod moves vertically and horizontally, respectively. The key difference in the respective motions is the range of angular pitching. This indicates that shell pitching is important for pteropod, and their swimming direction can be determined based on their dynamic angular orientation.

3.2.3 Parapodium ("wing") motion

During both power and recovery strokes, the parapodia elicit a reaction force from the fluid that causes the pteropod to propel. If the parapodium chord is aligned perpendicular to its motion, the reaction force is primarily drag. However, if the parapodium chord is oriented at an angle relative to its motion, the reaction force will constitute both lift and drag components. We examine the kinematics of the parapodia to determine whether the reaction force on the parapodia contains only a drag component (similar to paddling) or both drag and lift components.

The parapodium motion of the pteropod is analyzed by considering a two-dimensional projection of the chord viewed from a plane parallel to the sagittal plane of the vertically swimming pteropod (Fig. 10a). The parapodium flapping orientation of an upward swimming pteropod is examined relative to a translating and rotating reference frame (Fig. 10b), and a translating reference frame (Fig. 10c). These reference frames are calculated by subtracting the translational (and rotational) displacement of the pteropod shell. It should be noted, however, that Fig. 9 was described with respect to a stationary reference frame. Figure 10bi, ci show the trajectories of the parapodium during one complete cycle. The black dashed line is the trajectory of the chord midpoint of the distal end of the parapodium (see Fig. 1b), and the blue and green arrows describe the projected chord orientation during power and recovery strokes, respectively. In Fig. 10bi, we observe that the power stroke begins by moving the parapodium to a higher elevation followed by the parapodium flapping in a curved trajectory downwards. This is followed by a recovery stroke that returns the parapodium in a nearly horizontal trajectory to the beginning position of the power stroke. In Fig. 10bi, we observe that the strokes are not strictly reciprocal. The vertical distance between the power and recovery stroke trajectories is attributed to the ability of the pteropod to move the distal end of the parapodium, to a limited extent, via up-and-down, anterior-to-posterior, and twisting motions. In these power and recovery stroke trajectories, the parapodium traverses at an angle relative to its motion, indicated by α_1 and α_2 for power and recovery strokes, respectively (Fig. 10bi). The observed angular orientations suggest that the force generated on the parapodium constitutes both lift and drag components. The parapodium also undergoes pronation and supination (i.e. changing the angle from α_2 to α_1 as the parapodium transitions from recovery to power stroke, and vice versa), which consistently directs the resultant force such that the lift force is oriented upwards.

When the trajectory of the parapodium is considered with respect to only translating (but not rotating) coordinate system (Fig. 10cii), we observe a different trajectory of the parapodium (see Fig. 10ci). This trajectory shows that the power and recovery strokes both flap downwards, which corroborates with our kinematics analysis (Figs. 8, 9). The trajectory is also consistent with a figure-eight wing trajectory, which is known to be an efficient form of lift generation utilized by insect flight (Wang 2005). Shell pitching highly influences the trajectory of the parapodia. By controlling the shell pitching, the pteropod can develop different parapodium trajectories that lead to variations in direction and magnitude of the resultant force on the parapodia (Lehmann and Pick 2007; Izraelevitz and Triantafyllou 2014).

3.3 Surrounding fluid velocity field

3.3.1 Evolution of flow structures

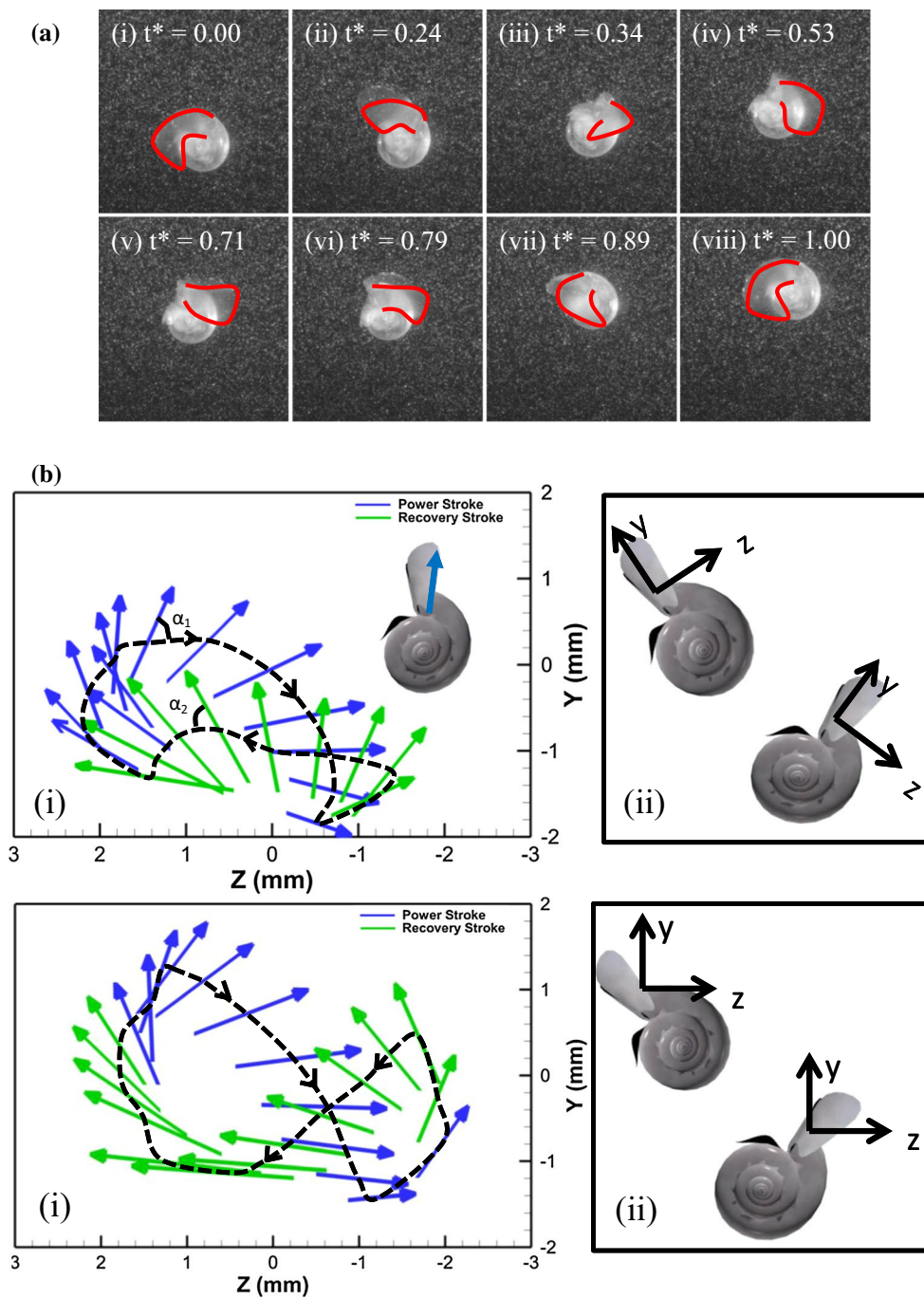The downward flapping during power and recovery stokes, together with the pronation and supination of the

Fig. 10 a Sagittal view of a time sequence of images of a vertically swimming pteropod from a stationary frame of reference. The parapodium is outlined in *red*. **b** The orientation and trajectory of the parapodium with respect to the translating and rotating frame of reference of a swimming pteropod (*inset* shows a schematic drawing of the pteropod with an illustration of the parapodium chord; also see Fig. 1). **c** The orientation and trajectory of the parapodium chord with respect to the translating, and not pitching, frame of reference. A schematic representation of the coordinate axes is shown in (*ii*) for both (**b**) and (**c**). The *dashed line* represents the trajectory of the midpoint of the distal end of the parapodium. The *blue* and *green arrows* represent the power and recovery strokes, respectively. α_1 and α_2 represent the angle of the distal end of the parapodium relative to its trajectory during power and recovery strokes, respectively

parapodia, can lead to flow patterns not observed in other swimming organism at intermediate *Re*. Here, we address the role that flow structures contribute to the acceleration of the organism.

Figure 11 shows a time sequence of the volumetric flow field surrounding the swimming pteropod, where the isosurface of vorticity magnitude of $|\omega| = 7$ s^{-1} is shown. Vorticity magnitude is used to illustrate the flow structures,
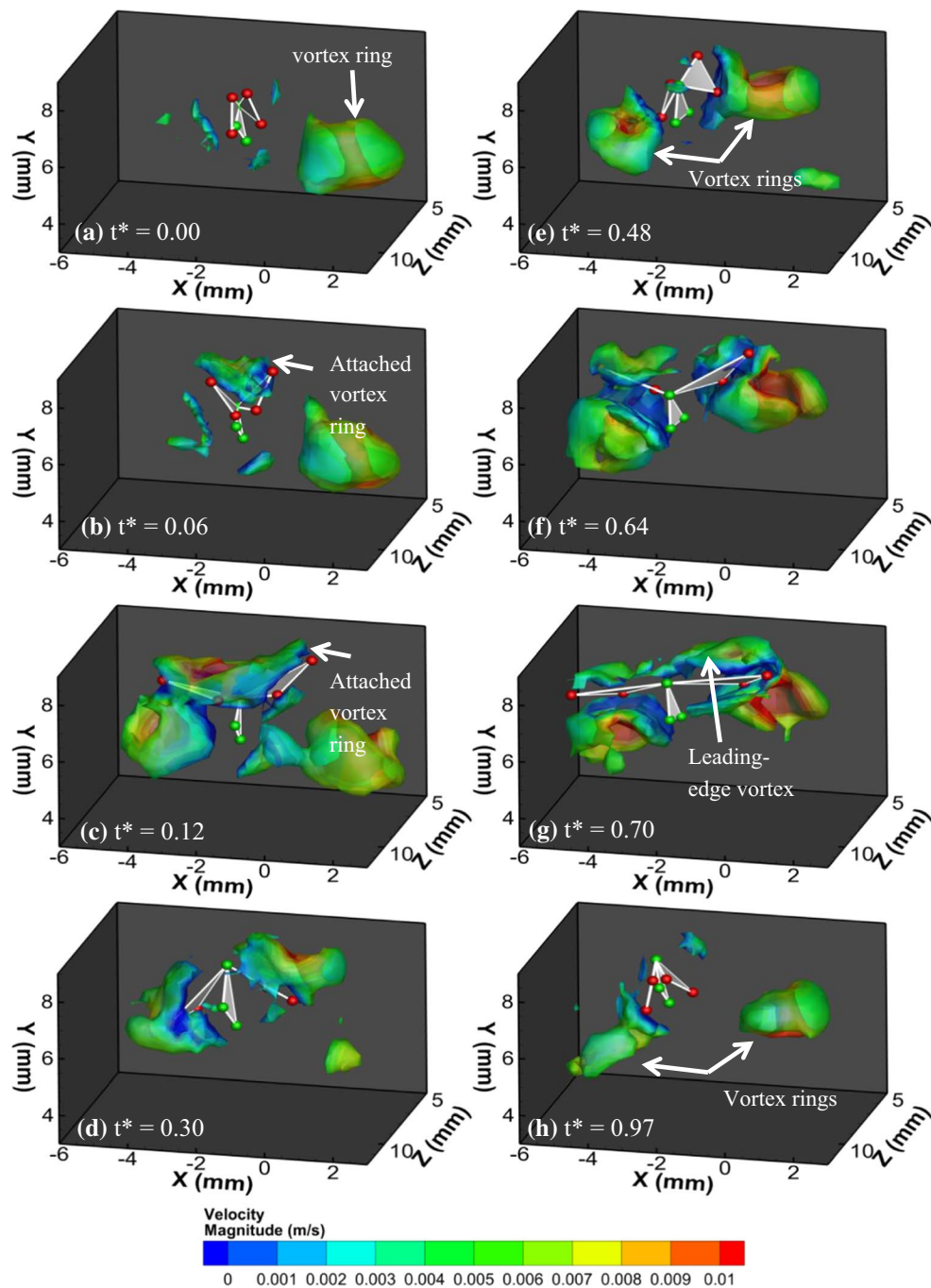
Fig. 11 Volumetric flow field of a swimming shelled Antarctic pteropod showing an iso-surface of vorticity magnitude ($|\omega| = 7 \text{ s}^{-1}$). An attached vortex ring and a leading-edge vortex are formed during power (**a**–**d**) and recovery (**e**–**h**) strokes, respectively. Power and recovery strokes both shed a pair of vortex rings in the wake of the organism, as shown in (**a**) and (**e**)

rather than other vortex identification schemes, because the organism is swimming at relatively low Reynolds number and does not necessarily generate a coherent swirl. Hence, iso-surfaces of vorticity are an appropriate representation of flow structures in this case. The orientation of the pteropod body is shown by three triangles, where the triangles with green and red vertices depict the shell and parapodia

positions, respectively. Figure 11a shows the start of the power stroke where the parapodia are close together. A vortex ring generated from the previous flapping cycle also is observed in Fig. 11a. The parapodia begin their power stroke by flapping downwards. During this process, an attached vortex ring connecting the leading- and trailing-edge vortex of the parapodia is observed (Fig. 11b), and
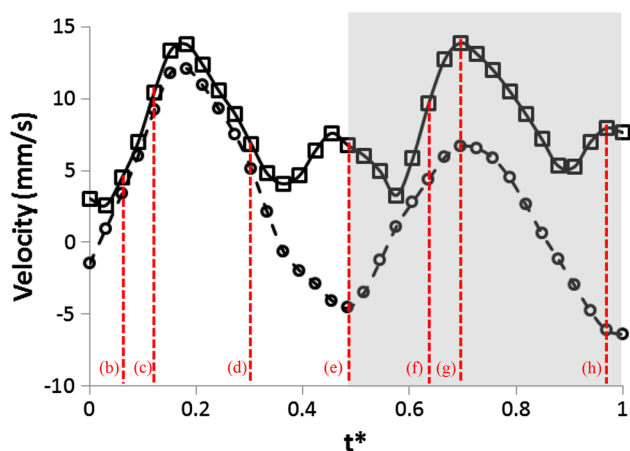
Fig. 12 Time record of the velocity magnitude (*solid line*, *square box*) and the vertical velocity component (*dashed line*, *circle*) of the swimming pteropod shown in Fig. 11. The *unshaded* and *shaded* areas represent the power and recovery strokes, respectively. The *letters* (*b*–*h*) correspond to the time points shown in Fig. 11

it sustains from $t* = 0.06$ to $t* = 0.20$ (Fig. 11c). Similar occurrence of an attached vortex ring developing on the top of the wings has been reported in the flight of aerial organisms (e.g. butterflies; Fuchiwaki et al. 2013; Langley et al. 2014). Toward the end of the power stroke, the attached vortex ring splits into a pair of vortex rings via a possible cut-and-reconnection process (Kida and Takaoka 1994; Saffman 1990) and the rings are shed into the wake of the pteropod (Fig. 11d, e). During the recovery stroke, the parapodia flap downwards again, and a leading-edge vortex is observed (Fig. 11f, g). This again leads to formation and shedding of a vortex ring into the wake of the pteropod as the parapodia move downward (Fig. 11h). The formation of the attached vortex ring during power stroke, formation of the attached leading-edge vortex during recovery stroke, and the shedding of vortex rings in the wake are consistent with other volumetric velocity fields of pteropods collected in this study.

3.3.2 Time record of swimming velocity

By comparing the vortex structures (Fig. 11) and the corresponding time record of velocity (Fig. 12) of the pteropod shell, we can relate the fluid motion around the pteropod to the forces generated on the pteropod during its flapping cycle. The largest acceleration (0.27 m/s^2) occurs at the beginning of the power stroke during the period of $t* = 0.03–0.15$ (determined from the slope of the time record of velocity magnitude in Fig. 12). This corresponds to time points in which the attached vortex ring is predominant (Fig. 11b, c), thus indicating a major role of the vortex ring in generating force on the pteropod. In addition, the vertical acceleration component determined by the slope of

the dashed line in Fig. 12 is similar to the total acceleration. This suggests that the attached vortex ring plays a significant role in the upward (*y*) component of acceleration. During the period $t* = 0.15–0.48$, the vertical velocity component decreases indicating a negative resultant acceleration due to the weight of the shell. The corresponding flow field sequence shows vortex rings shedding into the wake during this time period (Fig. 11d, e). At the beginning of the recovery stroke (Fig. 12; $t* = 0.48$), the vertical velocity component increases (dashed line; $t* = 0.48–0.70$) when the parapodia start to flap. This corresponds to the generation of a leading-edge vortex (Fig. 11f, g). In this time period, the velocity magnitude and the vertical component of velocity have a greater difference than that observed during the power stroke (Fig. 12). This suggests that the force generated on the pteropod has a significant horizontal component during the recovery stroke.

We find that the generation of the attached vortex ring and leading-edge vortex is crucial for vertical acceleration. This further supports the argument that significant lift force is generated from the parapodium motion. For aquatic organisms swimming at intermediate Reynolds number, utilizing lift-based propulsion is highly unusual. Most aquatic organisms in this Reynolds number regime exhibit paddling, jetting, or clapping (e.g. krill, salps, and scallops). Perhaps, the negatively buoyant shell necessitates higher thrust, which may be obtainable using both lift- and drag-based propulsion mechanisms as demonstrated by the shelled pteropods.

3.4 Comparison with shelled Pacific pteropods

The shelled Antarctic pteropod (*L. helicina antarctica*) may appear similar to shelled Pacific pteropod (*L. helicina*), but they have differences in their swimming behaviors and kinematics.

Table 1 shows the comparison of size and swimming characteristics of shelled Pacific and Antarctic pteropod based on Murphy et al. (2016) and the current work. We observe that the shelled Antarctic pteropod studied in the current work has (1) larger wing chord, (2) lower wingbeat frequency, and (3) larger pitching angle range, than shelled Pacific pteropods. The Reynolds number (Re_f) for both species is within the same intermediate regime, although we noted that Re_f for the Antarctica species is slightly larger. These differences in kinematic characteristics between the species may be attributed to the kinematic viscosity of the seawater in the Southern Ocean, which is 1.5 times higher than the Pacific Ocean. In order for both species to live in the same Reynolds number regime, the wing span and chord of the Antarctic pteropod must be larger than the Pacific pteropod. The larger wing chord for Antarctic pteropod is also required to maintain the necessary propulsive

Table 1 Comparison of size and swimming characteristics of shelled Pacific and Antarctic pteropods swimming vertically upwards

Species	Reference	Seawater temperature (°C)	Shell diameter (mm)	Wing chord (mm)	Swim speed (mm/s)	Wingbeat frequency (Hz)	Pitching angle range (deg.)	ν (mm²/s)	Re_f
Shelled Pacific pteropod	Murphy et al. (2016)	12	2.1–2.9	0.5–0.6	15–26	4.3–4.7	60	1.05	49–60
Shelled Antarctic pteropod	Current work	0	2.2	1.9	21	2.9	110	1.60	80

force at lower wingbeat frequency. Furthermore, the larger pitching angle attained through lower wingbeat frequency provides greater thrust in the upwards direction to overcome the larger drag force due to the higher viscosity of Antarctic seawater. Thus, the differences in wing chord, wingbeat frequency, and pitching angle suggests that shelled Antarctic pteropod have adapted to the higher seawater viscosity of their environment.

Murphy et al. (2016) observed a "near clap-and-fling" during the start of the power stroke for shelled Pacific pteropod. In Fig. 8 of the current work, we observed that the shelled Antarctic pteropod overlaps their parapodia at the beginning of the power stroke. However, the benefit of overlapping compared to "near clap-and-fling" is not clear from the current experimental results. Murphy et al. (2016) showed, for Pacific pteropods, a planar section of vortex pairs forming during the near clap-and-fling parapodia motion, and the evolution of the vortex pair downstream. The vortex pairs were speculated to be part of leading- and trailing-edge vortices. In the current work, Antarctic pteropod is found to swim in a similar Reynolds number regime and clear evidence of leading- and trailing-edge vortex tube formation is shown in Fig. 11 during both power and recovery strokes. Furthermore, the generation of these vortices corresponds to periods of high upward acceleration (Fig. 12). Thus, the current work validates and verifies the claim in Murphy et al. (2016) that the generation of leading- and trailing-edge vortices is indeed causing lift-based propulsion on shelled pteropods, and that these vortices eventually get shed into the wake as a pair of vortex rings.

3.5 Effects of ocean acidification on swimming shelled pteropods

Previous work has shown evidence of shell thinning of pteropods in the Antarctic or Arctic regions due to the effects of ocean acidification (OA) (Bednaršek et al. 2012; Comeau et al. 2012). The forces acting on the pteropod include thrust (F_{thrust}) by the parapodia, drag (F_{drag}) by the surrounding fluid, weight (F_{weight}) of the body, and buoyancy ($F_{buoyancy}$) due to the body volume. These forces, depicted
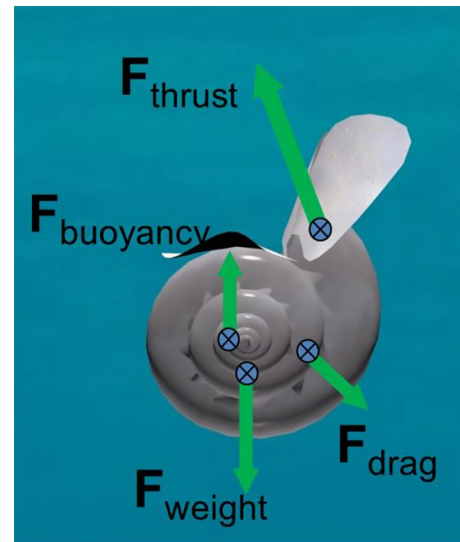

Fig. 13 Forces acting on the shelled Antarctic pteropod. F_{thrust} is the force generated by the flapping parapodia, $F_{buoyancy}$ is the buoyancy force on the body, F_{weight} is the weight of the body, and F_{drag} is the drag force. Ocean acidification thins the shell causing reduction in F_{weight} and, to a lesser extent, $F_{buoyancy}$

in Fig. 13, result in the pteropod translating upwards and to the left, while pitching in the counterclockwise direction due to the net moment.

Shell thinning by OA causes the weight and, to a limited extent, the buoyancy of the pteropod to decrease. However, the thrust and drag are unaffected directly by shell thinning. Thus, in response to shell thinning, the force balance will be altered, thereby affecting the motion and pitching characteristics of the pteropod shell. For instance, if F_{weight} decreases and F_{thrust} remains the same, the moment on the shell will increase. Furthermore, the reduced mass decreases the moment of inertia of the shell. The combined effect will lead to an increase in the angular acceleration during pitching, which will directly affect the wingbeat frequency and the extent of pitching angle. Since the wingbeat frequency and dynamic pitching angle determine the direction of the trajectory (as explained in Sect. 3.2), pteropod locomotion can be affected greatly by substantial shell

thinning. The shell may not be able to act as effective ballast, thereby causing the pteropod to be unstable in their locomotion.

With the persistence of OA, we predict that more pteropods will experience instability in the delicate balance of oscillatory pitching, flapping, and sawtooth-like trajectories. In the future, the locomotion characteristics of these pteropods, in fact, may provide an indication of the extent of OA.

4 Conclusion

In this study, we describe a portable tomographic PIV system that was transported and implemented successfully at Palmer Station, Antarctica, to study shelled Antarctic pteropods. These are important organisms to study because of their novel swimming characteristics and the potential for these characteristics to serve as indicators of ocean acidification. Our findings reveal that the pteropods flap their parapodia with both the power and recovery strokes directed downwards. This flapping characteristic is unique among intermediate Re aquatic propulsion and is facilitated by shell pitching, which reorients the parapodia to an elevated position after each stroke. The dynamic pitching angle range differs to facilitate either vertical or horizontal trajectories. The parapodia motion demonstrates pronation and supination that utilizes both drag and lift forces for propulsion. Furthermore, the parapodia follow a figure-eight trajectory, thus evidently employing a propulsion mechanism similar to small aerial organisms (e.g. insects) at intermediate Re. The volumetric fluid velocity field surrounding the pteropods shows an occurrence of an attached vortex ring and a leading-edge vortex on the parapodia during the power and recovery strokes, respectively. The attached vortex ring and leading-edge vortex correspond with higher acceleration, thus indicating relatively large forces acting on the organism during the development of these flow structures.

We find that the propulsion technique of a swimming shelled Antarctic pteropod is complex compared to most other organisms at intermediate Re that exhibit simpler propulsion technique (e.g. paddling, jetting, and clapping). Paddling, jetting, and clapping organisms predominantly utilize asymmetry in their propulsion. For example, krill retract their legs during the recovery stroke and extend them during the power stroke to paddle with a drag force, salps slowly draw in fluid and form rapid jets for propulsion, and scallops open their valves slowly and close rapidly to propel. For Antarctic pteropods, however, instead of flapping their parapodia in an asymmetric manner, they pitch their shell to orient the resultant force (both drag and lift) in the upwards direction. This complex swimming

behavior of shelled Antarctic pteropods is necessary to enable them to swim, maneuver, and hover in the intermediate Re regime.

Although Pacific pteropods were reported to pitch in a similar manner (Murphy et al. 2016), we find various differences with Antarctic pteropods. Shelled Antarctic pteropods have lower wingbeat frequency, larger wing chord, and larger pitching angle. However, the flow structures evolving for both Antarctic and Pacific species are similar since they swim within the intermediate Reynolds number regime. Thus, it appears that shelled Antarctic pteropods have adapted to the higher viscosity environment of the Southern Ocean.

Ocean acidification is (and will be) particularly pronounced in the Polar Regions and dissolves the shell of the pteropods, which reduces their weight and moment of inertia. The resulting altered balance of forces and pitching kinematics will affect locomotion for survival, feeding, and ultimately the fitness of the species. The current study serves as an initial understanding of pteropod swimming characteristics. Comparing these characteristics with shelled Antarctic pteropods in the near-future (i.e. with degraded shells) will enable us to definitively determine how their swimming is influenced by ocean acidification.

References

Adhikari D, Longmire EK (2012) Visual hull method for tomographic PIV measurement of flow around moving objects. Exp Fluids 53:943–964

Adhikari D, Longmire EK (2013) Infrared tomographic PIV and 3D motion tracking system applied to aquatic predator-prey interaction. Meas Sci Technol 24:024011

Adhikari D, Gemmell BJ, Hallberg MP, Longmire EK, Buskey EJ (2015) Simultaneous measurement of 3D zooplankton trajectories and surrounding fluid velocity field in complex flows. J Exp Biol 218:3534–3540

Bednaršek N, Tarling GA, Bakker DCE, Fielding S, Jones EM, Venables HJ, Ward P, Kuzirian A, Lézé B, Feely RA, Murphy EJ (2012) Extensive dissolution of live pteropods in the Southern Ocean. Nat Geosci 5:881–885

Casey TA, Sakakibara J, Thoroddsen ST (2013) Scanning tomographic particle image velocimetry applied to a turbulent jet. Phys Fluids 25:025102

Catton KB, Webster DR, Brown J, Yen J (2007) Quantitative analysis of tethered and free-swimming copepodid flow fields. J Exp Biol 210:299–310

Catton KB, Webster DR, Kawaguchi S, Yen J (2011) The hydrodynamic disturbances of two species of krill: implications for aggregation structure. J Exp Biol 214:1845–1856

Chang Y, Yen J (2012) Swimming in the intermediate Reynolds range: kinematics of the pteropod *Limacina helicina*. Integr Comp Biol 52:597–615

Cheng JY, DeMont ME (1996) Hydrodynamics of scallop locomotion: unsteady fluid forces on clapping shells. J Fluid Mech 317:73–90

Childress S, Dudley R (2004) Transition from ciliary to flapping mode in a swimming mollusc: flapping flight as a bifurcation in Re_ω. J Fluid Mech 498:257–288

Comeau S, Alliouane S, Gattuso J-P (2012) Effects of ocean acidification on overwintering juvenile Arctic pteropods *Limacina helicina*. Mar Ecol Prog Ser 456:279–284

Dabiri JO, Colin SP, Costello JH (2006) Fast-swimming hydromedusae exploit velar kinematics to form an optimal vortex wake. J Exp Biol 209:2025–2033

Elsinga GE, Scarano F, Wieneke B, van Oudheusden BW (2006) Tomographic particle image velocimetry. Exp Fluids 41:933–947

Flammang BE, Lauder GV, Troolin DR, Strand TE (2011) Volumetric imaging of fish locomotion. Biol Lett 7:695–698

Fuchiwaki M, Kuroki T, Tanaka K, Tababa T (2013) Dynamic behavior of the vortex ring formed on a butterfly wing. Exp Fluids 54:1450

Gattuso J-P, Hansson L (2011) Ocean acidification: Background and history. In: Gattuso J-P, Hansson L (eds) Ocean acidification. Oxford University Press, New York, pp 1–20

Gonzalez RC, Woods RE (2002) Digital image processing, 2nd edn. Prentice-Hall, New Jersey

Hedrick TL (2008) Software techniques for two- and three-dimensional kinematic measurements of biological and biomimetic systems. Bioinspir Biomim 3:034001

Howes EL, Bednaršek N, Büdenbender J, Comeau S, Doubleday A, Gallager SM, Hopcroft RR, Lischka Maas AE, Bijma J, Gattuso JP (2014) Sink and swim: a status review of thecosome pteropod culture techniques. J Plankton Res 36:299–315

Izraelevitz JS, Triantafyllou MS (2014) Adding in-line motion and model-based optimization offers exceptional force control authority in flapping foils. J Fluid Mech 742:5–34

Kida S, Takaoka M (1994) Vortex reconnection. Annu Rev Fluid Mech 26:169–189

Langley KR, Hardester E, Thomson SL, Truscott TT (2014) Three-dimensional flow measurements on flapping wings using synthetic aperture PIV. Exp Fluids 55:1831

Lauder GV (2015) Fish locomotion: recent advances and new directions. Annu Rev Mar Sci 7:521–545

Lauga E, Powers TR (2009) The hydrodynamics of swimming microorganisms. Rep Prog Phys 72:096601

Lehmann F-O, Pick S (2007) The aerodynamic benefit of wing-wing interaction depends on stroke trajectory in flapping insect wings. J Exp Biol 210:1362–1377

Lighthill MJ (1973) On the Weis-Fogh mechanism of lift generation. J Fluid Mech 60:1–17

Malkiel E, Sheng J, Katz J, Strickler JR (2003) The three-dimensional flow field generated by a feeding calanoid copepod measured using digital holography. J Exp Biol 206:3657–3666

Manno C, Morata N, Primicerio R (2012) *Limacina retroversa*'s response to combined effects of ocean acidification and sea water freshening. Estuar Coast Shelf Sci 113:163–171

Mendelson L, Techet AH (2015) Quantitative wake analysis of a freely swimming fish using 3D synthetic aperture PIV. Exp Fluids 56:135

Murphy DW, Webster DR, Yen J (2012) A high-speed tomographic PIV system for measuring zooplankton flow. Limnol Oceanogr Methods 10:1096–1112

Murphy DW, Webster DR, Yen J (2013) The hydrodynamics of hovering in Antarctic krill. Limnol Oceanogr Fluids Environ 3:240–255

Murphy DW, Adhikari D, Webster DR, Yen J (2016) Underwater flight by the planktonic sea butterfly. J Exp Biol 216:535–543

Orr JC, Fabry VJ, Aumont O, Bopp L, Doney SC, Feely RA, Gnanadesikan A, Gruber N, Ishida A, Joos F, Key RM, Lindsay K, Maier-Reimer E, Matear R, Mouchet A, Najjar RG, Plattner GK, Rodgers KB, Sabine CL, Sarmiento JL, Schlitzer R, Slater RD, Totterdell IJ, Weirig MF, Yamanaka Y, Yool A (2005) Anthropogenic ocean acidification over the twenty-first century and its impact on calcifying organisms. Nature 437:681–686

Saffman PG (1990) A model of vortex reconnection. J Fluid Mech 212:395–402

Scarano F, Poelma C (2009) Three-dimensional vorticity patterns of cylinder wakes. Exp Fluids 47:69–83

Sutherland KR, Madin LP (2010) Comparative jet wake structure and swimming performance of salps. J Exp Biol 213:2967–2975

Wang ZJ (2005) Dissecting insect flight. Annu Rev Fluid Mech 37:183–210

Weis-Fogh T (1973) Quick estimates of flight fitness in hovering animals, including novel mechanisms for lift production. J Exp Biol 59:169–230

Wieneke B (2008) Volume self-calibration for 3D particle image velocimetry. Exp Fluids 45:549–556